LA-UR-19-31259 (Accepted Manuscript)

Geodetic Measurements of Slow-Slip Events Southeast of Parkfield, CA

Delbridge, Brent G.
Carmichael, Joshua Daniel
Nadeau, Robert M.
Shelly, David R.
Burgmann, Roland

To be published in: Journal of Geophysical Research: Solid Earth

DOI to publisher's version: 10.1029/2019JB019059

Permalink to record: http://permalink.lanl.gov/object/view?what=info:lanl-repo/lareport/LA-UR-19-31259

JOURNAL OF GEOPHYSICAL RESEARCH, VOL. ???, XXXX, DOI:10.1029/,

Geodetic Measurements of Slow Slip Events Southeast of Parkfield, CA

Brent G. Delbridge,[1, 2] Joshua D. Carmichael,[3] Robert M. Nadeau,[1] David R. Shelly,[4] Roland Bürgmann[1]

Abstract. Tremor and low-frequency earthquakes are presumed to be indicative of surrounding slow, aseismic slip that is often below geodetic detection thresholds. This study uses data from borehole seismometers and long-baseline laser strainmeters to observe both the seismic and geodetic signatures of episodic tremor and slip on the Parkfield region of the San Andreas Fault near Cholame, CA. The observed occurrence rates of both the tremors and co-located families of low-frequency earthquakes are not steady, but instead exhibit quasi-periodic bursts of increased activity. We show that these periods of elevated seismic activity correlate with statistically significant stacked strain signals consisting of 44 slow slip events. Modeled individual slow slip events and their total summed moment, which are constrained by seismic signals and stacked strain respectively, indicate that the individual moment magnitudes of these events range from $M_w 4.6-5.2$. We find that the measured geodetic signal likely precedes the seismic signal by several hours, consistent with the aseismic slip preceding, and driving the observed seismic tremor activity. We confirm that strike-slip faults, in addition to subduction zones, are capable of producing episodic tremor and slip.

1. Introduction

The San Andreas fault (SAF) is one of the few strike-slip faults hosting tremors and low-frequency earthquakes (LFEs) [*Nadeau and McEvilly*, 2004; *Shelly*, 2017]. Both LFEs and tremors are associated with deep fault slip, and are thought to represent small embedded asperities which are driven to failure by otherwise aseismic slow slip within the surrounding fault [e.g. *Obara and Hirose*, 2006; *Shelly et al.*, 2006; *Peng and Gomberg*, 2010; *Rubinstein et al.*, 2007; *Thomas et al.*, 2018]. LFEs are repeating short-duration (seconds) seismic signals with identifiable phase arrivals resembling a traditional earthquake depleted in high frequencies [*Ide et al.*, 2007a; *Obara*, 2002], where as tremors are relatively long-duration (minutes) seismic signals lacking impulsive phase arrivals [*Nadeau and Dolenc*, 2005; *Shelly et al.*, 2007]. Further, LFEs are often observed to occur in rapid succession, and on the SAF are thought to comprise the majority of tremor signals [*Shelly*, 2017]. In contrast to the seismic component, aseismic fault slip is slow enough that inertial forces and thus seismic radiation are negligible. The durations of observed aseismic slip events range from minutes to decades, with displacements of up to tens of centimeters [e.g. *Peng and Gomberg*, 2010; *Bürgmann*, 2018]. In subduction zones, quasi-periodic burst of tremors accompanied by aseismic slip are referred to as episodic tremor and slip (ETS), and found to occur downdip of large locked fault zones where the fault is thought to transition from being fully locked to freely sliding [e.g. *Rogers and Dragert*, 2003; *Obara et al.*, 2004; *Obara and Kato*, 2016]. The goal of this study is to provide direct geodetic evidence of slow, aseismic slip in the Parkfield region of the strike-slip SAF during periods of increased seismic signals presumed to be indicative of aseismic slip events.

While the deep portion of the SAF is believed to be creeping, continuous monitoring of LFE activity on the Parkfield section of the SAF suggests a spatio-temporally complex deformation style *Shelly* [2017]. Stress transfer to the overlying locked patches may also lead to an increased probability of triggering a large event if this up-dip region is critically stressed [*Mazzotti and Adams*, 2004; *Beeler et al.*, 2016]. Understanding the stress accumulation and release in the Cholame region may provide valuable information about the seismic hazards associated with future ruptures analogous to the 2004 $M_w 6$ Parkfield and the 1857 $M_w 7.9$ Fort-Tejon Earthquakes.

In this study, we present an updated catalog of quasi-periodic tremor bursts which are thought to represent the seismic representation of ETS on the SAF [*Guilhem and Nadeau*, 2012]. The tremor catalog from which these quasi-periodic bursts of tremor were identified is compared with co-located LFEs [*Shelly*, 2017], and they are shown to exhibit similar spatio-temporal behavior. Regions containing a high density of located tremor are used to estimate the spatial extent of the slow slip source, and empirical scaling relations are used to estimate the total moment associated with the observed quasi-periodic bursts of tremors. Using these estimates of the moment release and slip area, the amount of slip associated with each quasi-periodic burst of tremor is estimated. Further, due to the high spatio-temporal resolution of LFE detections and their similarity to repeating earthquakes, the LFEs are used to develop a kinematic model of deep slow slip on the SAF in which the total cumulative slip is equal to the plate rate times the observational period. The source region is divided into discrete patches and the location and event timing of highly episodic low-frequency earthquake families are used as creepmeters to assign slip to the patches. This model is used to estimate a high-resolution timeseries of fault slip from which observable geodetic quantities such as surface strain are calculated. Both the empirical scaling relations (i.e. tremor

---

[1] Berkeley Seismological Laboratory, University of California, Berkeley, California, USA

[2] Dept. of Earth and Planetary Sciences, Harvard University, Cambridge, Massachusetts, USA.

[3] EES-17 (Geophysics), Los Alamos National Laboratory, Los Alamos, New Mexico, USA.

[4] Geologic Hazards Science Center, U.S. Geolgocial Survey, Golden, Colorado, USA.

0148-0227/20/$9.00

derived), and the kinematic model (i.e. LFE derived) yield consistent estimates of the slow slip magnitudes. The modeled synthetic strain timeseries is used to coherently stack the strain data from two nearby long-baseline laser strainmeters at times of modeled peak strain-rates.

Rousset et al. [2019] found GPS offsets associated with peaks of LFE activity to the northwest of Parkfield, using stacked GPS time series and a matched filter analysis, however, they where unable to resolve geodetic deformation for the Cholame area. We use long-baseline strainmeter measurements to observe and quantify the slow slip accompanying these large bursts of quasi-periodic tremors and LFEs on the Cholame section of the SAF. We confirm that similar to subduction zones, transform faults are capable of producing ETS.

2. Seismic Observations

2.1. Tremor Sources

We used borehole seismometer data from the High Resolution Seismic Network [*HRSN*, 2016] to locate tremors between 8/21/2001-6/1/2017 on the SAF beneath the northernmost rupture area of the M_w 7.8 Ft. Tejon earthquake of 1857 (Figure 1a). Using an envelope cross-correlation method [*Nadeau and Dolenc*, 2005; *Nadeau and Guilhem*, 2009], we located tremor sources (or tremors) to a depth range of $10-40$ km, with most tremors concentrating below the locked Cholame segment of the SAF. We find that the tremor durations are exponentially distributed with typical bursts lasting ∼5 to ∼20 minutes. Our tremor location uncertainties at the 95% confidence level are ±4.7 km and ±4.5 km in horizontal direction and depth respectively [*Nadeau and Guilhem*, 2009]. While the locations of the tremor sources appear to be located in a wide cloud around the SAF (Figure 1a), they are largely consistent with being located on the fault interface since the perpendicular distances from the fault are normally distributed about the fault interface with a standard of deviation of 4.6 km (Supplemental Figure S1). Further, *Guo et al.* [2017] show that by using a local 3-D v_s velocity model, and implementing a double-difference relocation scheme these tremors concentrate more strongly about the inferred fault interface. However, since the spatial distribution of tremors does not appear to be strongly elongated along fault (Figure 1a), and the distribution of tremor distances from the fault are too wide to be consistent with tremors only being located directly on the fault (Supplemental Figure S1), we cannot rule out the case that at least some of the tremor may be generated by off-fault sources which are distinct from those which generate the Cholame LFEs.

We denote a 25-km long portion of the SAF located within the high density cluster to the southeast of the rupture area of the 2004 M_w.0 Parkfield (black line, Figure 1a) at depths of $15-30$ km (black rectangle Figure 1b) as the "tremor source region". The temporal behavior of the tremors located with the tremor source region is not constant, but rather exhibits quasi-periodic bursts of high activity wherein the occurrence rate is >5 times the background rate which is measured as average tremor rate between the bursts (Figure 2a). Using the cross correlation method detailed in *Guilhem and Nadeau* [2012], we identify 82 burst episodes (Table 1), with recurrence intervals ranging from ∼ 30-150 days (Table 1). We find that individual burst episodes last 2 to 10 days. These short bursts account for about one third (33%) of all tremor detections and correspondingly, a similar fraction (31%) of the total measured tremor duration. The total measured tremor duration of each individual episode ranges from tens to hundreds of minutes of recorded coherent tremor (Table 1).

It has been established that there is a physical relationship between ETS and large earthquakes with a causal relationship possible in either direction; that is, ETS may trigger large earthquakes, and large earthquakes may trigger ETS via static stress transfer [*Obara and Kato*, 2016]. In the case of the 2004 Parkfield earthquake, there have been reports of elevated tremor and LFE activity prior to the mainshock [*Nadeau and Guilhem*, 2009; *Shelly*, 2009]. Following the 2004 Parkfield Earthquake, there was a large and persistent increase in the rate of tremor occurrence [*Nadeau and Guilhem*, 2009; *Shelly and Johnson*, 2011]. The average tremor occurrence rate increased from ∼1.5 min/day to ∼5 min/day during the 100 days following the earthquake. In addition, the peak episode rates increased from 6.64 ± 0.9 to 9.10 ± 1.8 min/day. These results are consistent with those of previous studies which carefully examined the response of tremors and LFEs to the 2004 Parkfield Earthquake [e.g. *Nadeau and Dolenc*, 2005; *Nadeau and Guilhem*, 2009; *Shelly and Johnson*, 2011].

The largest burst of tremor is observed directly following the M_w6.0 2014 Napa Earthquake, which occurred nearly 350 km to the northwest. The peak rate that directly followed the mainshock was 23 min/day, about 10 times the background rate, and twice the average peak rate, where the average peak rate is measured as the mean tremor duration of the identified burst episodes (Figure 2a). The elevated peak tremor burst rates following the 2014 Napa Earthquake slowly decayed at a rate of -0.04 min/day while the background tremor rate remained elevated (∼4.5 min/day) from August 2014 though the end of the observational period in June 2017 (Figure 2b).In addition to elevated rates, the periodicity of the bursts also increased and became more regular.

To put these changes in context, we note that there are significant variations in the background rate prior to the earthquake. Following a lull in tremor activity that began in 2013, there was an acceleration in tremor activity beginning in July, 2014, prior to the occurrence of the 2014 South Napa Earthquake. We also examined the tremor response to all earthquakes that occurred within 350 km of the Cholame region a year before and after the 2014 Napa Earthquake, and find additional peaks in the tremor rate that appear to be associated with regional seismicity (vertical dashed lines, Supplemental Figure S2). We note two events of particular interest which are associated with large rapid increases in tremor rate, a M_w 4.5 earthquake which occurred ∼150 km away in Central California on Nov. 20, 2014, and a pair of M_w 4.5 and M_w 4.7 earthquakes which occurred approximately 300 km away on the California-Nevada border region on Feb. 11, 2014.

2.2. Low-Frequency Earthquakes (LFEs)

The LFE catalog of *Shelly* [2017] contains more than one million LFEs which are associated with 88 families, approximately half of which are located on the Cholame segment of the SAF (Black Box, Figure 1b). The LFEs are located on or very close to the SAF fault interface (Figure 1). The template matching approach used for LFE detection [*Shelly*, 2009] is reminiscent of the methodology and assumptions used for the detection of repeating earthquakes [*Uchida and Bürgmann*, 2019]. Consequently, LFEs are thought to be analogous to repeating earthquakes which occur on small fault zone asperities with failure being driven by aseismic fault slip on the surrounding fault interface [*Uchida and Bürgmann*, 2019]. Additionally, focal mechanisms of P-wave first motions and moment tensors using S waves from LFEs found in subduction zone settings show that those events represent shear slip on the plate interface [*Ide et al.*, 2007b]. Further, the SAF LFEs have been shown to occur preferentially during times when tidal stresses encourage right-lateral shear slip [*Thomas et al.*, 2012, 2016]. The precise spatio-temporal identification, proximity to the fault interface, and shear slip mechanisms make LFEs good indicators of fault slip at depth.

We examine the temporal behavior of the LFEs located within the tremor source region(black box shown in Figure 1). Similar to our results for the tremor behavior, we observe that the LFEs exhibit quasi-periodic bursts of high activity which persist for 2-10 days, with the burst rates exceeding on average 5 times the background rate (average rate during inter-burst periods, see Supplemental Figure S3). However we also note that the episodicity is highly variable, and the LFE distribution is more continuous at greater depths, suggesting less ETS-like accelerations. Many of the families that are highly episodic, with activity that tends to occur in bursts rather than at regular intervals, are clustered within the red rectangle in Figure 1, and denoted by warm colors. The more than one hundred thousand episodic LFEs we use represent 10% of the total SAF LFE catalog, and 23% of the LFEs located along the Cholame segment. These, highly episodic families have been shown to be particularly robust creepmeters *Thomas et al.* [2018].

Similar to the tremors, the largest increase in LFE rate occurred in response to the M_w 6.0 2014 Napa Earthquake [*Peng et al.*, 2015]. *Peng et al.* [2015] argue that the spatio-temporal propagation of LFE activity during the large burst initiating 12 hours after the mainshock reflects a large triggered slow slip event. The LFE peak directly following the mainshock of this event has an amplitude of $\sim$ 900 LFEs/day, which reflects an increase of 30 times the background rate, and twice the average peak rate (Supplemental Figure S4). Similar to the observed tremor rates, the peak rates following the Napa Earthquake remain elevated, and decay at similar rates (Supplemental Figures S4 and S5). However, in contrast to the significant increase in background tremor rate observed after the Parkfield earthquake, we only observe a $\sim$ 1% in the background LFE rate (Supplemental Figures S4 and S5). Similar to the observed background tremor rates prior to the Napa Earthquake, we also observe a steady decrease in the background LFE rate beginning in $\sim$ 2013. This decrease in background LFE rate culminates in a $\sim$3-month period of quiescence from December 2014 to February 2015, following which the background LFE occurrence rate returns to its pre-Napa levels. This decrease in background LFE rate is marked by a period of decreased LFE detection due to low-correlation values [*Shelly*, 2017], and is coincident with increased background tremor levels. However, it is difficult to compare these observations with the change in the background LFE rate following the Parkfield Earthquake due to gain changes in the HRSN in 2003, which reduced overall noise levels [*Shelly*, 2017]. Since there are no static stress changes imposed by the Napa Earthquake, we expect the response to differ significantly from that of the Parkfield Earthquake.

3. Geodetic Detection

The 82 quasi-episodic episodes identified using cross-correlation (Table 1), represent periods of increased lower-crustal seismic activity (i.e., LFE and tremor occurrence rates) well above the background rate, and are localized in the region in Figure 1. While there is ample micro-seismic evidence (tremors and LFEs) to support episodic aseismic slip on the deep extent of the Cholame SAF, there has previously been no observable geodetic evidence to support this inference [*Smith and Gomberg*, 2009; *Rousset et al.*, 2019]. Due to the similarity of these quasi-periodic bursts with ETS and slow slip in subduction zones, we propose a simple model to explore the mechanics of this process and to predict the size of these candidate ETS events. The surface deformation associated with these inferred slow slip events is estimated by modeling them as deep shear dislocations, where the geometry of the slipping region is defined by the region of high tremor density and locations of the low-frequency earthquake sequences. The location and timing of highly episodic low-frequency earthquake families is used to assign slip to the discretized portions of the source region such that there is no net strain stored over the observational period. Using the modeled surface deformation and modern geodetic instrumentation, we devise a procedure to overcome the obstacle faced by previous studies in order to detect the geodetic signal associated with these proposed slow-slip events. *Rousset et al.* [2019] were not able to resolve a GPS signal along the Cholame section of the SAF, likely due to the low strains thought to be associated with these events. However, long-baseline laser strainmeters (LSM) and borehole strainmeters (BSM) are thought to be capable of measuring the small magnitude surface geodetic signals associated with these short-duration slow-slip events [*Agnew and Wyatt*, 2003]. Due to the proximity and stability of the LSM Figure 1, the high noise levels present in the Parkfield BSMs and the failures of previous targeted attempts to observe these signals [*Smith and Gomberg*, 2009], we will only focus on the LSMs.

In Section 3.1 we estimate the cumulative and average SSE slip only using constraints on the fault slip rate and tremor-derived estimates of the source geometry and recurrence intervals (A and T_R, Table 1), under the assumption that all slip in the source region is accommodated during the seismically inferred slow slip events. We then independently use the measured tremor durations to estimate the source magnitude using an empirical relationships derived for ETS in the Cascadia subduction zone. Section 3.2 then uses the highly-episodic LFEs as creepmeters, and distributes the moment estimated in Section 3.1 spatially and temporally to discrete patches on the plate interface. This spatiotemporal distribution of slip is then used to calculate synthetic surface strain times series. Sections 3.3-3.5 then use the seismic observations to guide the stacking of strain data, using the model developed in Section 3.2, in order to geodetically validate the modeled SSEs in Section 3.1.

3.1. Estimation of Slow-Slip Magnitude

The deformation at depth ($>$ 14km) is assumed to be accommodated entirely by the quasi-periodic slow-slip events that accompany the observed bursts of micro-seismic energy, and the amount of slip released in these events maintains the average plate sliding rate (or plate rate), such that there is no net stored strain. The long-term SAF slip rate in the vicinity of the proposed slow-slip zone, at depths below $\sim$14 km, is $\sim$33mm/yr [*Ryder and Bürgmann*, 2008].

In order to maintain plate rate over the duration of the observational period, the slow slip events must release a cumulative slip of $\sim 512\,\mathrm{mm}$ (Duration $\times$ plate rate= 15.5 yr $\times$ 33 mm yr^{-1}). If all events are assumed to be equal, then the slip associated with an individual ETS event is $\sim 6\,\mathrm{mm}$ such that that the slip is equally divided amongst the 82 identified episodes. However, in order to account for the inter-event time differences the amount of slip d is assumed to be equal to the tectonic loading rate ($\dot{S}$) times the recurrence interval preceding the slow-slip event (T_R, Table 1)

$$d = T_R \dot{S}. \quad (1)$$

This results in uniform slip (d) over the entire slow-slip region (A), which is exactly equal to the slip deficit accumulated from preceding tectonic loading.

The total moment release of the slow slip events is given as

$$M_0 = \mu A d, \quad (2)$$

where μ is the shear modulus (here assumed to be 30GPa), A the area of the slow-slip plane in meters squared, and d is the amount of slip in meters accommodated by all ETS and background activity. For ease of comparison, we convert event moments to moment magnitudes

$$M_w = \frac{2}{3}\log_{10}\left(M_0 \cdot 10^7\right) - 10.7, \tag{3}$$

where M_0 is given in newton meters (N·m).

Assuming a constant deep fault slip-rate ($\dot{S}$), and a fixed slow-slip area associated with Model 1 (20 km by 5 km) of 100 km^2 (red rectangle, Figure 1b), or Model 2 (25 km by 15 km) of 375 km^2 (black rectangle, Figure 1b), the calculated cumulative slip results in a cumulative moment magnitude release of 6.2 M_w and 6.5 M_w, and average individual event magnitudes of 4.8 M_w and 5.2 M_w respectively. The slips and moment magnitudes estimated for each individual slow-slip event are reported in columns 4-6 of Table 1. These values strongly depend on the assumed area of the slow-slip event and the amount of slip accommodated by background activity between the 82 events. While the geodetic surface deformation from several millimeters of slip at this depth may be too small to detect from a single individual event ($\sim 5M_w$), we may be able to observe the cumulative geodetic moment release through proper stacking to utilize the full moment release.

Alternatively, it has been observed in both Japan and Cascadia that the geodetic moment release is linearly proportional to the cumulative duration of tremor during a slow-slip event [*Aguiar et al.*, 2009; *Obara et al.*, 2010]. The empirical relation uses the estimated duration of tremor in hours (T_D, Table 1) to estimate the geodetic moment release. In northern Cascadia, this relationship was estimated as [*Aguiar et al.*, 2009]

$$M_0 = 5.2 \cdot 10^{16} T_D. \tag{4}$$

Applying this empirical relation to the total cumulative duration of tremor (151.2hours), results in a cumulative moment release of $7.2 \cdot 10^{18}$ or 6.5 M_w. This estimate is at the upper bound of the the estimate based purely on recurrence interval T_R. The moment-duration estimated moment magnitude (M_w) for each episode is given in column 5 of Table 1. These magnitude estimates refer to the inferred slow slip driving the activity on the small seismic patches, rather than the slip, and the moment of the seismic patches themselves, which can be smaller by several orders of magnitude [*Kao et al.*, 2010].

3.2. Modeled Surface Deformation

Following *Thomas et al.* [2018], we use the highly episodic LFE families as creepmeters to quantify the deep slip-rate. In order to calculate the expected surface deformation associated with these inferred ETS events, we discretize the slipping patches (solid red and black rectangles, Figure 1) into patches of five km length (dashed red and black rectangles, Figure 1) and normalize the slip assigned to each LFE such that the cumulative slip from each patch is equal to the plate rate times the observational period. The slip of the i^{th} patch is calculated by weighting the cumulative slip (S_{total}) by the number of LFEs within the patch (L_i) and the total number of occurrences for the j^{th} family (N_j). Thus the slip s_{ij} assigned to the i^{th} patch associated with an occurrence of the j^{th} LFE family is:

$$s_{ij} = \frac{S_{Total}}{N_i L_j}. \tag{5}$$

The total fault slip time series is constructed by adding the contribution of each episodic family such that the j^{th} occurrence of that LFE family represents an amount of slip s_{ij} (Equation 5) on the i^{th} patch (Figure 1b) that contains it. The corresponding surface deformation is then calculated using a rectangular 3D Okada dislocation corresponding to each patch's geometry and fault slip time series [*Okada*, 1985; *Thompson*, 2014].

One year (2012) of the modeled north-south synthetic strain time series calculated at the location of a nearby long-baseline laser-strainmeter (LSM, purple triangle, Figure 1) is shown in Figure 3 (The full time series over the observational time period for the North-South and East-West components of strain are shown in Supplemental Figure S6). The total cumulative North-South and East-West surface strain associated with the LFE-inferred deep-fault slip over the $\sim$ 15.5 year observation period is on the order of a few micro-strain, and the strain associated with any one given slow-slip episode is on the order of several nano-strain (Figure 3a). While the total cumulative surface strain is not large due to the depth of the inferred aseismic slip, there are significant rate variations that we expect to be observable at the surface (Figure 3b). The bottom panel of Figure 3 shows the strain-rate calculated using a 2 day smoothing window. Recall that while all of the surface strain is associated with deep fault slip, the quasi-periodic episodes of accelerated slip characterized by peaks in strain-rate are what we refer to as slow-slip events. Note that the inter-event deformation is not zero (Figure 3a). By using the LFEs as creepmeters, we capture both the deformation associated with the quasi-periodic bursts and the inter-event background creep, which we neglected in our "back of the envelope" estimates in the previous section. The mean strain-rates of the slow-slip events are larger by a factor of $\sim$ 3.5 over the mean background strain-rate, and the maximum strain-rate is associated with the episode triggered by the 2014 M6.0 Napa earthquake. Note that the amplitude of the surface strain is strongly dependent on the moment and the distribution of that moment with depth, however, since the lateral extent of the slip region is largely the same, the synthetic time series for Model 2 is linearly proportional to Model 1, with Model 2 = 3.85 · Model 1. Model 1 has one third the moment of Model 2, corresponding to the smaller depth range of 20 - 25 km versus 15 - 30 km.

3.3. Deformation Detection Levels

The deep-fault slip model (section 3.2) predicts surface deformation signals with amplitudes on the order of 10's of nano-strain with durations ranging from 1 to 10 days. Surface geodetic deformation measurements are of differential displacement with borehole strainmeters measuring over baselines of 10^{-4} km, long-baseline strainmeters over baselines of $10^{-1} - 10^{0}$ km, and GPS over baselines of $10 - 10^{3}$ km. The detection level of various geodetic instruments are largely set by environmental noise levels, and thus the deformation detection levels of these geodetic instruments are a function of the period of the desired signal we wish to measure [*Agnew*, 1992]. At short periods (days or less) borehole strainmeters have the best performance (i.e. lowest detection threshold), and at longer periods (greater than a year) GPS instruments have the best performance. However, at intermediate periods (days to months) the long-baseline strainmeters are the most suitable instrument [*Agnew and Wyatt*, 2003]. At periods of one week, long-baseline strainmeters show wander rates that are a $\sim$ 100 times smaller than GPS, and $\sim$ 10 smaller than borehole strainmeters. For a full description of instrument wander, we refer to [*Agnew and Wyatt*, 2003].

3.4. The Cholame Long-baseline Laser Strainmeters

In order to detect the geodetic signature of the the slow-slip events (Section 3 and Section 3.2), we use strain data from the two Cholame long-baseline laser strainmeters, conveniently located near the slow-slip region(Figure 1a). We use strain time series with five-minute sampling rate spanning September 4, 2008 to August 27, 2018. The two co-located instruments (CHL1 and CHL2) are oriented to measure strain in the North-South (CHL1) and East-West (CHL2) directions. These long-baseline laser strainmeters are half-kilometer-long interferometers which use laser light to measure the change in the relative position of two monuments. Figure 4 shows one year (2012) of raw LSM derived North-South strain data (red curve), and the corrections applied to the data (blue and grey curves). There exist three main sources of error which affect laser-strain measurements: (1) variation in optical path length, (2) changes in laser frequency over time and (3) local motion of the end point monuments. The motion of the monuments is by far the largest source of error, and is mitigated by measurements from "optical anchors" [*Wyatt et al.*, 1982] which are installed at both end points. The blue curve in Figure 4 represents the corrections estimated for both end point monuments of the LSM. Corrections for variations in the strength of vacuum, changes in laser frequency, and effects of temperature and pressure are estimated to be an order of magnitude smaller than the tidal correction, and several orders of mangitude smaller than the optical anchor correction (grey curve, Figure 4). The next largest signals present in the data are from the tides, which are shown by the purple curve in Figure 4. After removing all corrections and tides, we are left with signal which we refer to as the "observed strain" shown by the black curve in Figure 4. We note however, that the long-baseline laser strain meters are very sensitive to hydrological deformation caused in response to rainfall. The optical anchors mitigate this hydrological effect and attempt to remove the local deformation near the end point monuments, however, for some rain large rain events the optical anchors are not able to fully mitigate this deformation signal, leaving large hydrological signals ($>$ 10 nano-strain) in the data (e.g. Supplemental Figure S7).

3.5. Observed Surface Strain

We identify strain-rate peaks from the synthetic strain timeseries, and then align and stack the signals from the corresponding strain data (Figure 5). The LSM was in operation and able to capture 49 of these events. Five of these time periods were excluded from analysis due to large excursions that are not associated with deep slow slip and are likely related to local hydrology and precipitation (Supplemental Figure S8). In order to increase our ability to detect the small surface strain signals associated with these events, we first bandpass filter the observed strain data between 1 and 20 days using a fourth-order Butterworth filter, to remove spurious signals, such as hydrological deformation, and increase the signal-to-noise ratio of the expected signal we are attempting to observe. We then select 25 days of the filtered observed strain before and after the peak strain-rate estimated from the modeled synthetic strain time series (Figure 5). We then detrend the 50 day strain data segment only using the first 15 days of the time series (Figure 5).

We then stack 44 of the 50 day periods aligned on the peak strain rate, which have a signal-to-noise greater than 10 (See Appendix A). We note that this additional data quality check was employed in order to ensure that our stacked signal is not dominated by spurious large-amplitude signals, which can be on the order of tens to hundreds of nano-strain (i.e., the large offsets around 2012-10 in Figure 4 and Supplemental Figures S7 and S8). Figure 6 shows the resulting average stack of 44 aligned chunks of filtered LSM-derived observed strain data for both the North-South and East-West components (yellow curves). The average stacks of the corresponding filtered Model 1 and Model 2 synthetic strains are shown by the thick and thin dashed black lines (Figure 6).

4. Discussion

The modeled synthetic strain stack is in good agreement with the observed geodetic strain (solid yellow and dashed black curves, Figure 6), with the exception of a brief excursion several days following the time of the inferred slow-slip events ($\sim$ 8 days), which is not explained by our simple LFE model. We find that the lower-magnitude Model 1 fits the data better than Model 2, suggesting that the slow-slip region more-closely corresponds to the smaller area denoted by the red rectangle in Figure 1. In order to test the robustness of this result we perform a jackknife test to estimate both the mean and variance of the observation, and importantly, since this an average stack we want to ensure that the observation is not dependent on only a few observational time periods. To perform the jackknife test, we randomly remove 10% of the 50-day filtered observed strain samples (i.e., five observations from each component) and re-calculate the average stack. A thousand realizations of the jackknife test are plotted as semi-transparent black curves in Figure 6. For each time step we calculate the variance and mean of all the jackknife observations. The mean and 2σ bounds are plotted as red and blue curves in Figure 6, however the mean (red curve) is mostly hidden by the yellow curve since it is nearly identical to the full stack average.

To further ensure that our stacked results are not biased by our processing scheme, or generated by random chance, we generate synthetic stacks using random peak times. We use the same processing steps and data selection criterion that was used to create the stacks shown in Figure 6. We then measure the misfit of the generated random stack with the modeled stack, using two metrics 1) the normalized RMS misfit and 2) the misfit of the mean long-term offset. We then generate 10^4 random stacks and estimate the random distribution for both metrics. The resulting probability and cumulative distributions are shown in Figure 7. Using metric 1 (normalized RMS misfit) the observed geodetic strain is more than 2σ different from the random distribution. Further, no single realization of the random stacks can match the long-term offsets of both components (Figure 7b), suggesting that we cannot create the observed offsets randomly.

In summary, the stacked strain results are consistent with the source area defined by the highly episodic LFEs (Model 1) exhibiting quasi-periodic slow-slip events, and the slip-history of this region being well described by using the highly episodic LFEs as creepmeters (e.g. [*Thomas et al.*, 2018] and Section 3.2). Both the tremors and LFEs in the Chalome region exhibit quasi-periodic bursts of increased activity associated with these geodetically observed slow-slip events.

4.1. Statistical Significance

In order to further assess the statistical significance of our detection we developed a formal hypothesis test which is detailed in Appendix A. We applied this test with a digital signal detector against the observed and aligned stack of observed strain-rate (as opposed to strain). This detector tests between the competing hypotheses that the strain-rate either does not show a tectonic signal above expected background variability (only noise), or that the strain-rate includes a significant signal that is elevated above this noisy background. This statistical procedure uses the same peak times and data processing steps as Section 3, with the key differences being that an additional step is taken to calculate the strain-rate, a more rigorous definition of "statistical significance" is developed, and we determine if the strain data is temporally shifted relative to our modeled time series.

We process our observed strain data with a finite difference method over time and normalize the result to assess the distributional form of the observed observed strain-rate. The resulting histograms revealed that our unstacked observed strain-rate signal is dominated by a random background field that includes normally distributed, Gaussian noise.

Having determined that random background strain-rate values dominate our unstacked, post-processed observed strain-rate records, we then tested our stacked data. We ran our detector (Equation A7) on randomized stacks of 44 strain-rate realizations, $\sim 10^4$ times (Figure A1a). This statistic again showed some spurious peaks that we could mostly attribute to end-of-file mismatches. We then fit our predicted $\mathcal{F}$ PDF to normalized histograms of the binned detection statistic to estimate its distributional parameters and threshold for detection; we chose a threshold to be consistent with a rate of one false alarm per 10 years of strain-rate data (Figure A1b). We then aligned and stacked our strain-rate data using the peak times from the LFE derived Model 1 following the procedure detailed in Section 3.5. The detection statistic that we computed from this stacked data showed a maximum near the time of peak modeled strain-rate where it exceeded our threshold, and indicates that this stack represents a geodetic signal that is unlikely to be present in the background strain-rate field (Figure A2).

Finally, we evaluated the choice of our temporal alignment at peak modeled strain. Specifically, we determined if stacking the 44 observed strain-rate signals after aligning them with other phase shifts could elevate or depress detection rates, since a subsequent absence of any detection could indicate weakened evidence for a geodetic signal. We sampled temporal phase shifts uniformly distributed over ± 2 days (based on the LFE and tremor burst durations, Figures 3), shifted our data, and stacked the results. This test showed that some small shifts (mostly phase shifts near $\pm +4$ hrs) elevated the presence of a geodetic signal (larger $z(\dot{\epsilon})$. Larger shifts (many phase shifts nearly ± 2 days) depressed the presence of a geodetic signal so that $\sim 10\%$ of stacked and shifted data produced no detectable geodetic signal. This phase-shift and stack exercise revealed that more optimal phase shifts produced a 15 dB geodetic signal. This result suggests that aligning our data to peak modeled strain-rate is sub-optimal, and refined phase shifting and stacking can significantly improve our ability to detect a geodetic signal. To test if phase shifted stacking on noise could similarly result in a geodetic signal, we duplicated our test 10^4 times on 10^3 randomized realizations background strain-rate records of equal duration. This latter exercise produced no detections on random realizations of strain-rate data (Figure A3). This improvement in detection arises from the fact that these small temporal shifts improve the coherency of our data stacks that include signal, but do not improve coherency between realizations of a random background field. We conclude that a random superposition of background observed strain-rate realizations is unlikely to produce a geodetic signal that triggers our detector at its threshold.

Cumulatively, our hypothesis test shows that a geodetic signal that is aligned to our peak model strain-rate ($\pm <$ 2 days) has $< 0.1\%$ probability (a one in a ten-thousand chance) of being observed in expected background strain. We therefore accept the hypothesis that our stacked data reveal a geodetic signal and thus conclude that we have recorded transient strain-rate signals that are geodetic evidence of slow slip deep on the SAF near Chalome.

5. Conclusions

We have used borehole seismometer data from the High Resolution Seismic Network and Tremor Scope to resolve tremors between 8/21/2001-6/1/2017 on the SAF beneath the rupture area of the M7.8 Ft. Tejon earthquake of 1857. We observe that the tremor rate is not constant but shows quasi-periodic bursts of high activity wherein the burst rates exceed the background rate by ∼5 times. We find that the largest burst of tremor observed in our data set represents a ten-fold increase in the tremor rate and likely reflects a response to the 2014 M6.0 Napa Earthquake that is located nearly 350 km to the northwest. The long-term average tremor occurrence rate following this event increased significantly ($> 150\%$) and remained elevated throughout the duration of the observational period, however, this persistent increase is not observed in the LFE occurrence rate. We speculate that while tremor and low-frequency earthquakes are intimately related, in practice, the highly-episodic repeating low-frequency events are directly recording slip on the plate interface, whereas the tremor may represent both deformation on the fault interface and possibly, distinct off-fault deformation associated with slow slip. Whether the differences between the spatial distribution, temporal evolution and response to external forcing of tremors and LFEs result from differences in detection algorithms and network status or whether they represent distinct indicators of the physical state of the fault zone remains elusive and requires further study.

We identified 82 quasi-period bursts using cross-correlation [i.e. *Guilhem and Nadeau*, 2012], which represent periods of increased seismic activity (i.e. LFE and tremor occurrence rates) that are well above the background rate, and that are localized to the slow-slip region. The recurrence intervals of these events range from 30 to 150 days, with individual burst durations ranging from 2 to 10 days.

We identify highly episodic low-frequency earthquake families from the catalog of *Shelly* [2017], which are located within the source region of the resolved episodic burst of tremor. We assume that these highly episodic LFEs may be used as creepmeters [*Thomas et al.*, 2018], and are analogous to repeating earthquakes that occur on small fault zone asperities, with failure being driven by aseismic fault slip on the surrounding fault interface [*Uchida and Bürgmann*, 2019]. The amount of aseismic slip assigned to the surrounding fault that drives the LFE failure is scaled to match the total slip expected during the full observation period. Assuming a fixed slow-slip area (A) of 100 km^2 (Figure 1b), and constant deep fault slip-rate ($\dot{S}$), the calculated cumulative slip of 512.4 mm / 15.5 yr times 33 mm/yr results in a cumulative moment release or $1.9 \cdot 10^{18}$ or 6.2 M_w. We estimate the surface deformation associated with these events by discretizing the inferred slow-slip zone into five patches and use a rectangular Okada dislocation model to estimate the associated surface strain. By stacking the strain records from the long-baseline laser strain-meters, we are able to observe the average surface geodetic deformation associated with these events and conclude that these large bursts of tremor activity are accompanied by geodetically detectable slow-slip. This positive result warrants revisiting the BSM instruments, despite their increased sensitivity to environmental and hydrological noise, and ought to provide a fruitful avenue for future research.

We develop several statistical tests to determine the significance of these observations, and conclude that there is less than a one in ten-thousand chance of a false detection. Further, our detection statistic indicates that the measured geodetic slip proceeds the modeled slip (Figure A2), which is causally consistent with the aseismic slip proceeding and driving the LFE activity. Additionally, small temporal shifts improve the coherency of our data stacks, with an optimal mean shift of +4.8 hours, suggesting that the onset of geodetic slip may proceed the seismic signature of slip by a period of several hours. However, we are unable to resolve whether this precursory slip occurs within, or adjacent to, the tremor source region.

In summary, we find that the Cholame region of the strike-slip San Andreas Fault produces seismically and geodetically observable ETS of magnitudes of M_w $4.8 - 5.2$.

Table 1: Identified quasi-Episodic tremor burst episode characteristics. Column 1: Peak correlation time. Column 2: Tremor recurrence interval T_R measured in days since previous episode. Column 3: Duration of tremor burst T_D measured in minutes of observed seismic tremor. Column 4: Amount of slip associated with each burst based on recurrence interval. Column 5-6: Moment magnitudes based on the slip d and source areas of Model 1 and Model 2 respectively. Column 7: Moment magnitude based on the empirical moment to tremor duration scaling of *Aguiar et al.* [2009].

	T_R(day)	T_D(min)	d(mm)	$M_W^{(A1)}$	$M_W^{(A2)}$	$M_W^{(Emp.)}$
2001-10-20	-	46.1	-	-	-	5.0
2001-12-08	49.20	61.7	4.4	4.7	5.1	5.1
2002-01-07	36.70	93.2	3.3	4.6	5.0	5.2
2002-02-03	56.90	104.0	5.1	4.8	5.1	5.3
2002-05-11	61.00	50.2	5.5	4.8	5.2	5.1
2002-06-28	47.00	50.0	4.2	4.7	5.1	5.1
2002-11-05	130.30	85.0	11.8	5.0	5.4	5.2
2003-01-03	58.80	65.7	5.3	4.8	5.2	5.1
2003-04-23	110.00	108.2	9.9	4.9	5.3	5.3
2003-08-05	104.70	53.4	9.5	4.9	5.3	5.1
2003-09-05	30.30	48.8	2.7	4.6	5.0	5.1
2003-10-25	50.00	43.5	4.5	4.7	5.1	5.0
2004-01-01	69.10	57.8	6.2	4.8	5.2	5.1
2004-03-28	86.20	109.3	7.8	4.9	5.3	5.3
2004-05-02	35.50	54.6	3.2	4.6	5.0	5.1
2004-06-29	57.80	54.7	5.2	4.8	5.1	5.1
2004-09-07	69.50	184.9	6.3	4.8	5.2	5.4
2004-10-08	31.30	294.9	2.8	4.6	5.0	5.6
2005-01-16	45.10	73.2	4.1	4.7	5.1	5.2
2005-01-24	108.00	78.6	9.8	4.9	5.3	5.2
2005-02-28	34.80	120.3	3.1	4.6	5.0	5.3
2005-04-25	55.70	180.9	5.0	4.8	5.1	5.4
2005-07-25	46.00	189.2	4.2	4.7	5.1	5.4
2005-09-18	55.10	96.7	5.0	4.7	5.1	5.2
2005-11-27	70.20	85.4	6.3	4.8	5.2	5.2
2006-01-03	63.50	137.9	5.7	4.8	5.2	5.4
2006-01-18	62.10	94.8	5.6	4.8	5.2	5.2
2006-04-28	88.50	92.7	8.0	4.9	5.3	5.2
2006-09-15	78.00	58.6	7.1	4.9	5.2	5.1
2006-12-01	76.40	112.5	6.9	4.8	5.2	5.3
2007-02-18	79.20	122.0	7.2	4.9	5.2	5.3
2007-05-07	77.80	127.7	7.0	4.8	5.2	5.3
2007-07-17	71.20	70.7	6.4	4.8	5.2	5.2
2007-10-06	81.10	162.7	7.3	4.9	5.2	5.4
2008-01-11	97.00	159.4	8.8	4.9	5.3	5.4
2008-05-05	116.00	124.6	10.5	5.0	5.3	5.3
2008-09-10	127.00	175.1	11.5	5.0	5.4	5.4
2008-12-18	99.10	134.8	9.0	4.9	5.3	5.3
2009-02-21	65.10	59.8	5.9	4.8	5.2	5.1
2009-04-15	52.90	147.1	4.8	4.7	5.1	5.4
2009-06-14	60.10	128.6	5.4	4.8	5.2	5.3
2009-08-10	56.80	84.5	5.1	4.8	5.1	5.2
2009-09-28	49.20	173.1	4.4	4.7	5.1	5.4
2009-11-03	35.90	125.0	3.2	4.6	5.0	5.3
2010-01-02	78.90	109.0	7.1	4.9	5.2	5.3
2010-03-17	55.90	88.5	5.1	4.8	5.1	5.2
2010-06-30	105.10	49.0	9.5	4.9	5.3	5.1
2010-09-03	64.10	114.3	5.8	4.8	5.2	5.3
2010-10-29	56.90	47.8	5.1	4.8	5.1	5.0
2010-12-28	59.60	103.8	5.4	4.8	5.2	5.3

2011-01-03	32.60	97.2	2.9	4.6	5.0	5.3
2011-01-07	40.10	77.1	3.6	4.7	5.0	5.2
2011-01-23	97.90	186.1	8.9	4.9	5.3	5.4
2011-05-12	62.30	94.9	5.6	4.8	5.2	5.2
2011-12-02	106.30	80.9	9.6	4.9	5.3	5.2
2012-01-03	80.50	32.6	7.3	4.9	5.2	4.9
2012-01-04	68.30	97.0	6.2	4.8	5.2	5.2
2012-04-28	79.20	37.8	7.2	4.9	5.2	5.0
2012-06-16	48.50	85.3	4.4	4.7	5.1	5.2
2012-08-06	51.00	69.8	4.6	4.7	5.1	5.2
2013-01-15	80.80	136.4	7.3	4.9	5.2	5.3
2013-01-25	109.00	25.0	9.9	4.9	5.3	4.9
2013-02-20	36.30	72.7	3.3	4.6	5.0	5.2
2013-05-21	90.70	60.6	8.2	4.9	5.3	5.1
2013-10-09	31.20	76.8	2.8	4.6	5.0	5.2
2014-01-02	103.00	81.1	9.3	4.9	5.3	5.2
2014-02-21	32.00	60.6	2.9	4.6	5.0	5.1
2014-04-25	62.90	98.7	5.7	4.8	5.2	5.3
2014-06-10	46.60	108.1	4.2	4.7	5.1	5.3
2014-08-26	76.30	297.6	6.9	4.8	5.2	5.6
2014-11-20	86.10	324.5	7.8	4.9	5.3	5.6
2015-02-18	89.90	232.2	8.1	4.9	5.3	5.5
2015-05-05	76.20	126.6	6.9	4.8	5.2	5.3
2015-06-24	49.80	183.5	4.5	4.7	5.1	5.4
2015-10-22	120.50	204.6	10.9	5.0	5.4	5.5
2016-03-03	132.30	181.4	12.0	5.0	5.4	5.4
2016-06-05	94.60	141.5	8.6	4.9	5.3	5.4
2016-07-20	45.00	70.2	4.1	4.7	5.1	5.2
2016-08-28	38.20	164.7	3.5	4.6	5.0	5.4
2016-11-01	64.60	148.2	5.8	4.8	5.2	5.4
2017-01-15	75.10	166.4	6.8	4.8	5.2	5.4
2017-04-28	102.80	101.5	9.3	4.9	5.3	5.3

Appendix A: Hypothesis Tests on the Significance of Geodetic Signal

Following the same data processing steps as Section 3.5, we detrend and bandpass filter both channel records (CHL1 and CHL2) of the observed strain with a first order, zero phase, Butterworth filter. Our usage of the term “signal” herein does not presume that our post-processed data includes a geodetic signature aside from that present in the background strain-rate field. We term such background strain-rate features as non-target signals, and transient geodetic features in the stacked data that are not noise as “target signals”. We emphasize these tests process strain-rate $\dot{\epsilon}$ rather than strain ϵ data.

We first assess the distributional form of the post-processed, background observed strain-rate. We estimate time-derivatives with a finite difference approximation that exploits the method of undetermined coefficients [*LeVeque*, 2007]. We then bin and normalize the post-processed strain-rate data to form empirical density functions (histograms). The resulting histograms show an approximately Gaussian distribution that includes heavy tails and indicates that our data are punctuated by occasional, large amplitude peaks. We find that these peaks mostly result from finite differences between sample mismatches at the ends-of-files resulting from the concatenation of year-long time series. These histograms reveal that our unstacked observed strain-rate signal is dominated by a random background field that includes normally distributed, zero-mean Gaussian noise of variance σ^2 (that is, $\dot{\epsilon} \sim \mathcal{N}\left(0, \sigma^2\right)$). Thus we assume that our stacked strain-rate data are sufficiently Gaussian and compare two competing hypotheses ($\mathcal{H}_0$ versus $\mathcal{H}_1$) at each time sample t:

$$\begin{aligned} &\mathcal{H}_0 : \dot{\epsilon}(t) = n \sim \mathcal{N}\left(0, \sigma^2\right), \quad \text{versus:} \\ &\mathcal{H}_1 : \dot{\epsilon}(t) = \dot{s} + n \sim \mathcal{N}\left(\dot{s}, \sigma^2\right). \end{aligned} \tag{A1}$$

Our binary hypothesis test (Equation A1) models the observed observed strain-rate data $\dot{\epsilon}$ at time t as either a Gaussian field with zero mean (hypothesis $\mathcal{H}_0$), or as a Gaussian field with mean $\dot{s}$ (hypothesis $\mathcal{H}_1$). We assume that the noise variance σ^2 is unknown under $\mathcal{H}_0$. Similarly, we assume that the sum of the target signal variance and the background strain-rate variance is unknown under $\mathcal{H}_1$. To make this hypothesis test more tractable, we mark a change in the total variance at an unknown time with t_S. We physically interpret this time to index the appearance a strain-rate signal in the stack. Equation A1 is then equivalent to:

$$\begin{aligned} &\mathcal{H}_0 : \ \sigma^2(t < t_S) = \sigma^2(t > t_S), \quad \text{versus:} \\ &\mathcal{H}_1 : \ \sigma^2(t < t_S) < \sigma^2(t > t_S) \end{aligned} \tag{A2}$$

We derive a test statistic $z\left(\dot{\epsilon}\right)$ from these competing hypotheses as a generalized likelihood ratio test on our strain-rate data that is identical in form to a test statistic for a generalized short-term to long-term average (STA/LTA) detector [e.g. *Arrowsmith et al.*, 2015; *Marcillo et al.*, 2019; *Carmichael and Nemzek*, 2019]. In other words, the statistical test of Equation A2 compares the sample variance estimate $\hat{\sigma}_1^2$ of the observed strain-rate in a leading, short term window, to the sample variance estimate $\hat{\sigma}_0^2$ of the observed strain in a following, long-term window as:

$$z(\dot{\epsilon}) = \frac{\hat{\sigma}_1^2}{\hat{\sigma}_0^2} \sim \mathcal{F}_{\hat{S},\hat{L}}\left(\lambda\right) \tag{A3}$$

in which $z \sim \mathcal{F}_{\hat{S},\hat{L}}\left(\lambda\right)$ indicates that the detection statistic z is distributed as a noncentral $\mathcal{F}$ random variable with degrees of freedom $\hat{S}$ and $\hat{L}$ and noncentrality parameter λ. The quantities $\hat{S}$ and $\hat{L}$ relate to the data as the effective number of statistically independent samples in the short-term window (S samples long) and the effective number of independent samples in the long-term window (L samples long), respectively. The best parameter estimates are positive scalars $\hat{S}$ and $\hat{L}$ that minimize the norm of the difference between a normalized data histogram of $z(\dot{\epsilon})$ and discretized central $\mathcal{F}$ PDF:

$$[\hat{S}, \hat{L}] = \underset{S,L}{\operatorname{argmin}} \left|\left| \text{Hist}(z(\dot{\epsilon}))|_{0.05}^{99.5} - f_Z\left(z; \mathcal{H}_0\right) \right|\right| \tag{A4}$$

where $\text{Hist}(z)|_{0.05}^{99.5}$ bins excludes data outside the upper and lower 0.5% quantiles. The resultant histogram misfit e:

$$e = \left|\left| \text{Hist}(z(\dot{\epsilon}))|_{0.05}^{99.5} - f_Z\left(z; \mathcal{H}_0\right) \right|\right| \Big|_{\hat{S},\hat{L}} \tag{A5}$$

measures our confidence in how well $\mathcal{F}_{\hat{S},\hat{L}}$ represents the data. The parameter λ is proportional to the standard definition of the signal-to-noise ratio (SNR) of the target signal that is included in the short term window at times $t > t_S$:

$$\lambda = \text{SNR} \cdot (S - 1), \tag{A6}$$

where $\text{SNR} = \sum_k^S \dot{s}_t^2 \ / \ \sum_t^S n_t^2$ (t is time sample). Under the null hypothesis $\mathcal{H}_0$, $\lambda = 0$ (no signal present), and under $\mathcal{H}_1$, $\lambda > 0$. Our geodetic target signal detector tests this detection statistic for evidence of geodetic signal as a decision rule that chooses $\mathcal{H}_1$ if $z(\dot{\epsilon})$ meets or exceeds a threshold η ($z(\dot{\epsilon}) \geq \eta$) and chooses $\mathcal{H}_0$ if the threshold exceeds the statistic ($z(\dot{\epsilon}) < \eta$):

$$z(\dot{\epsilon}) \underset{\mathcal{H}_0}{\overset{\mathcal{H}_1}{\gtrless}} \eta. \tag{A7}$$

Our detector defines the threshold η from a constant false-detection constraint. This constraint relates the threshold to the probability $\text{Pr}_{FA} = C$ (typically, $C < 10^{-2}$) of erroneously deciding $\mathcal{H}_1$ when $\mathcal{H}_0$ is true as $\eta = F_Z^{-1}\left(1 - C, \mathcal{H}_0\right)$, where $F_Z^{-1}\left(z, \mathcal{H}_0\right)$ is the inverse, central $\mathcal{F}$ cumulative distribution function (CDF) for $z \sim \mathcal{F}_{\hat{S},\hat{L}}\left(0\right)$. The CDF should not be confused with the random variable notation. With this threshold selection, the probability Pr_D that the detector in Equation A7 detects a geodetic signal with a given SNR is:

$$\text{Pr}_D = 1 - F_Z\left(\eta; \mathcal{H}_1\right), \tag{A8}$$

in which $F_Z\left(z; \mathcal{H}_1\right)$ is the noncentral $\mathcal{F}$ CDF for $z \sim \mathcal{F}_{\hat{S},\hat{L}}\left(\text{SNR}\left(S-1\right)\right)$; again, the CDF should not be confused the the random variable for z. In practice, λ and the SNR under $\mathcal{H}_1$ in Equation A6 are each unknown. The following estimate $\hat{\lambda}$ for λ uses post-detected statistics to determine the signal strength of any geodetic signal in the stack of a observed strain-rate signal [*Carmichael and Nemzek*, 2019, Equation A11]:

$$\begin{aligned} &\hat{\lambda} = z(\dot{\epsilon}) \left(\frac{\hat{S}}{\hat{L}}\right) \left(\hat{L} - 2\right) - \hat{S}, \\ &\text{where: } z(\dot{\epsilon}) > \eta, \end{aligned} \tag{A9}$$

so that $\text{SNR} \approx \frac{\hat{\lambda}}{\hat{S}}$. We select S to be 5 days to scale with LFE and tremor burst duration, and L to exceed twice this duration (L = 10 days). Other sources more fully document more general details of our detector's implementation [*Carmichael and Nemzek*, 2019, Appendix A].

Having determined that random background strain-rate values dominate our unstacked, post-processed observed strain-rate records, we then tested our stacked data. We ran our detector (Equation A7) on randomized stacks of 44 strain-rate realizations, $\sim 10^4$ times (Figure A1a). This statistic again showed some spurious peaks that we could mostly attribute to end-of-file mismatches. The remaining peaks that were not artifacts agreed in number with the false alarm rate of our detector, for each particular detector run. We therefore accepted these data as consistent with our data model, and assembled degree-of-freedom estimates ($\hat{S}$, $\hat{L}$, Equation A3) that we computed for each detector run and estimated the ensemble parameter mean and variance (we performed a bootstrap). The bootstrap process showed very low variances in our empirical parameter estimates and instilled further confidence in the hypothesized distributional form of our detection statistic. We selected the error-weighted average of $\hat{S}$ and $\hat{L}$ over all such runs to parameterize a central $\mathcal{F}$ PDF (N total runs, runs indexed by k):

$$[\hat{S}, \hat{L}] = \frac{\sum_k^N e_k^{-1}[\hat{S}_k, \hat{L}_k]}{\sum_k^N, e_k^{-1}} \tag{A10}$$

where e is defined in Equation A5 defines and thereby compute a threshold for detection that was consistent with a $\mathrm{Pr}_{FA} = \frac{1}{300}$ false alarm rate (see text after Equation A7). We chose this false alarm rate to roughly agree with one false alarm per 10 years of strain-rate data processing(Figure A1b):

$$\frac{1/300\,\mathrm{FA}}{1\,\mathrm{window}} \cdot \frac{1\,\mathrm{window}}{14\,\mathrm{days}} \cdot \frac{365\,\mathrm{days}}{1\mathrm{yr}} < \frac{0.09\,\mathrm{FA}}{\mathrm{yr}} \tag{A11}$$

We then aligned and stacked our strain-rate data using the peak times from the LFE derived Model 1 following the procedure detailed in Section 3.5. We then stacked observed strain-rate signals recorded 25 days prior to this peak modeled strain-rate and 25 days after peak modeled strain, for each of 44 distinct burst events.The detection statistic that we computed from this stacked data showed a maximum near the time of peak modeled strain-rate where it exceeded our threshold, and indicates that this stack represents a geodetic signal that is unlikely to be present in the background strain-rate field (Figure A2). To further assess the significance of this peak, we collected 10^3, 10^2 day samples of random, post-processed observed strain-rate signals and re-applied our detector. 0.08% of this data produced peaks that exceeded our threshold. These spurious peaks (detections) are again consistent with the expected false alarm rate of the detector.

Finally, we evaluated the choice of our temporal alignment at peak modeled strain. Specifically, we determined if stacking the 44 observed strain-rate signals after aligning them with other phase shifts could elevate or depress detection rates, since a subsequent absence of any detection could indicate weakened evidence for a geodetic signal. We sampled temporal phase shifts uniformly distributed over ±2 days (based on the LFE and tremor burst durations, Figure 3), shifted our data, and stacked the results. This test showed that some small shifts (mostly phase shifts near $\pm +4$ hrs) elevated the presence of a geodetic signal (larger $z\,(\dot{\epsilon})$. Larger shifts (many phase shifts nearly ±2 days) depressed the presence of a geodetic signal so that $\sim$ 10% of stacked and shifted data produced no detectable geodetic signal. This phase-shift and stack exercise revealed that more optimal phase shifts produced a 15 dB geodetic signal. This result suggests that aligning our data to peak modeled strain-rate is sub-optimal, and refined phase shifting and stacking can significantly improve our ability to detect a geodetic signal. To test if phase shifted stacking on noise could similarly result in a geodetic signal, we duplicated our test 10^4 times on 10^3 randomized realizations background strain-rate records of equal duration. This latter exercise produced no detections on random realizations of strain-rate data (Figure A3). This improvement in detection arises from the fact that these small temporal shifts improve the coherency of our data stacks that include signal, but do not improve coherency between realizations of a random background field. We conclude that a random superposition of background observed strain-rate realizations is unlikely to produce a geodetic signal that triggers our detector at its threshold.

Cumulatively, our hypothesis test shows that a geodetic signal that is aligned to our peak model strain-rate ($\pm <$ 2 days) has $< 0.1\%$ probability (a one in a ten-thousand chance) of being observed in expected background strain. We therefore accept the hypothesis that our stacked data reveal a geodetic signal and thus conclude that we have recorded transient strain-rate signals that are geodetic evidence of slow slip deep on the SAF near Chalome.

Acknowledgments. Support for R.M.N. was provided by NSF through Award #1460498. Support for B.G.D. was provided from the NSF Graduate Research Fellowship under grant DGE1106400. The Nuclear National Security Agency and Leslie Casey supported J.D.C. We thank Dave Mencin, Joan Gomberg and an anonymous reviewer for comments and suggestions which greatly improved the manuscript. We recognize Duncan Agnew and Frank Wyatt for their tireless efforts to design, build and maintain the LSM instruments. Data for this study come from the High Resolution Seismic Network (HRSN) doi:10.7932/HRSN, operated by the UC Berkeley Seismological Laboratory, which is archived at the Northern California Earthquake Data Center (NCEDC), doi: 10.7932/NCEDC. This material is based on services provided by the GAGE Facility, operated by UNAVCO, Inc., with support from the National Science Foundation and the National Aeronautics and Space Administration under NSF Cooperative Agreement EAR-1724794. All data used in this study are publicly available. The seismic data is available for download from NCEDC web services (https://www.ncedc.org/SeismiQuery/) and the long-baseline laser strainmeter data are available from UNAVCO web services (https://www.unavco.org/data/strain-seismic/lsm-data/lsm-data.html).

References

Agnew, D. C. (1992), The time-domain behavior of power-law noises, *Geophysical research letters*, *19*(4), 333–336.

Agnew, D. C., and F. K. Wyatt (2003), Long-base laser strainmeters: a review, *SIO Technical Report 2*.

Aguiar, A. C., T. I. Melbourne, and C. W. Scrivner (2009), Moment release rate of cascadia tremor constrained by gps, *Journal of Geophysical Research: Solid Earth*, *114*(B7).

Arrowsmith, S., G. Euler, O. Marcillo, P. Blom, R. Whitaker, and G. Randall (2015), Development of a robust and automated infrasound event catalogue using the international monitoring system, *Geophysical Journal International*, *200*(3), 1411–1422.

Beeler, N., G. Hirth, A. Thomas, and R. Bürgmann (2016), Effective stress, friction, and deep crustal faulting, *Journal of Geophysical Research: Solid Earth*, *121*(2), 1040–1059.

Bürgmann, R. (2018), The geophysics, geology and mechanics of slow fault slip, *Earth and Planetary Science Letters*, *495*, 112–134.

Carmichael, J. D., and R. J. Nemzek (2019), Uncertainty in the predictive capability of detectors that process waveforms from explosions, *arXiv preprint arXiv:1906.09350*.

Guilhem, A., and R. M. Nadeau (2012), Episodic tremors and deep slow-slip events in central california, *Earth and Planetary Science Letters*, *357*, 1–10.

Guo, H., H. Zhang, R. M. Nadeau, and Z. Peng (2017), High-resolution deep tectonic tremor locations beneath the san andreas fault near cholame, california, using the double-pair double-difference location method, *Journal of Geophysical Research: Solid Earth*, *122*(4), 3062–3075.

HRSN (2016), High resolution seismic network, dataset. doi:10.7932/HRSN.

Ide, S., G. C. Beroza, D. R. Shelly, and T. Uchide (2007a), A scaling law for slow earthquakes, *Nature*, *447*(7140), 76–79.

Ide, S., D. R. Shelly, and G. C. Beroza (2007b), Mechanism of deep low frequency earthquakes: Further evidence that deep non-volcanic tremor is generated by shear slip on the plate interface, *Geophysical Research Letters*, *34*(3), doi: 10.1029/2006GL028890.

Kao, H., K. Wang, H. Dragert, J. Y. Kao, and G. Rogers (2010), Estimating seismic moment magnitude (mw) of tremor bursts in northern cascadia: Implications for the seismic efficiency of episodic tremor and slip, *Geophysical Research Letters*, *37*(19).

LeVeque, R. J. (2007), *Finite difference methods for ordinary and partial differential equations: steady-state and time-dependent problems*, vol. 98, Siam.

Marcillo, O., S. Arrowsmith, M. Charbit, and J. Carmichael (2019), Infrasound signal detection: re-examining the component parts that makeup detection algorithms, in *Infrasound Monitoring for Atmospheric Studies*, pp. 249–271, Springer.

Mazzotti, S., and J. Adams (2004), Variability of near-term probability for the next great earthquake on the cascadia subduction zone, *Bulletin of the Seismological Society of America*, *94*(5), 1954–1959.

Nadeau, R. M., and D. Dolenc (2005), Nonvolcanic tremors deep beneath the san andreas fault, *Science*, *307*(5708), 389–389.

Nadeau, R. M., and A. Guilhem (2009), Nonvolcanic tremor evolution and the san simeon and parkfield, california, earthquakes, *science*, *325*(5937), 191–193.

Nadeau, R. M., and T. V. McEvilly (2004), Periodic pulsing of characteristic microearthquakes on the san andreas fault, *Science*, *303*(5655), 220–222.

Obara, K. (2002), Nonvolcanic deep tremor associated with subduction in southwest japan, *Science*, *296*(5573), 1679–1681.

Obara, K., and H. Hirose (2006), Non-volcanic deep low-frequency tremors accompanying slow slips in the southwest japan subduction zone, *Tectonophysics*, *417*(1), 33–51.

Obara, K., and A. Kato (2016), Connecting slow earthquakes to huge earthquakes, *Science*, *353*(6296), 253–257.

Obara, K., H. Hirose, F. Yamamizu, and K. Kasahara (2004), Episodic slow slip events accompanied by non-volcanic tremors in southwest japan subduction zone, *Geophysical Research Letters*, *31*(23).

Obara, K., S. Tanaka, T. Maeda, and T. Matsuzawa (2010), Depth-dependent activity of non-volcanic tremor in southwest japan, *Geophysical Research Letters*, *37*(13).

Okada, Y. (1985), Surface deformation due to shear and tensile faults in a half-space, *Bulletin of the seismological society of America*, *75*(4), 1135–1154.

Ozacar, A. A., and G. Zandt (2009), Crustal structure and seismic anisotropy near the san andreas fault at parkfield, california, *Geophysical Journal International*, *178*(2), 1098–1104.

Peng, Z., and J. Gomberg (2010), An integrated perspective of the continuum between earthquakes and slow-slip phenomena, *Nature Geoscience*, *3*(9), 599–607.

Peng, Z., D. R. Shelly, and W. L. Ellsworth (2015), Delayed dynamic triggering of deep tremor along the parkfield-cholame section of the san andreas fault following the 2014 m6. 0 south napa earthquake, *Geophysical Research Letters*, *42*(19), 7916–7922.

Rogers, G., and H. Dragert (2003), Episodic tremor and slip on the cascadia subduction zone: The chatter of silent slip, *Science*, *300*(5627), 1942–1943.

Rousset, B., R. Bürgmann, and M. Campillo (2019), Slow slip events in the roots of the san andreas fault, *Science advances*, *5*(2), eaav3274.

Rubinstein, J. L., J. E. Vidale, J. Gomberg, P. Bodin, K. C. Creager, and S. D. Malone (2007), Non-volcanic tremor driven by large transient shear stresses, *Nature*, *448*(7153), 579.

Ryder, I., and R. Bürgmann (2008), Spatial variations in slip deficit on the central san andreas fault from insar, *Geophysical Journal International*, *175*(3), 837–852.

Shelly, D. R. (2009), Possible deep fault slip preceding the 2004 parkfield earthquake, inferred from detailed observations of tectonic tremor, *Geophysical Research Letters*, *36*(17).

Shelly, D. R. (2017), A 15 year catalog of more than 1 million low-frequency earthquakes: Tracking tremor and slip along the deep san andreas fault, *Journal of Geophysical Research: Solid Earth*, *122*(5), 3739–3753.

Shelly, D. R., and K. M. Johnson (2011), Tremor reveals stress shadowing, deep postseismic creep, and depth-dependent slip recurrence on the lower-crustal san andreas fault near parkfield, *Geophysical Research Letters*, *38*(13), doi: 10.1029/2011GL047863, l13312.

Shelly, D. R., G. C. Beroza, S. Ide, and S. Nakamula (2006), Low-frequency earthquakes in shikoku, japan, and their relationship to episodic tremor and slip, *Nature*, *442*(7099), 188.

Shelly, D. R., G. C. Beroza, and S. Ide (2007), Non-volcanic tremor and low-frequency earthquake swarms, *Nature*, *446*(7133), 305–307.

Smith, E. F., and J. Gomberg (2009), A search in strainmeter data for slow slip associated with triggered and ambient tremor near parkfield, california, *Journal of Geophysical Research: Solid Earth*, *114*(B12).

Thomas, A., R. Bürgmann, D. R. Shelly, N. M. Beeler, and M. Rudolph (2012), Tidal triggering of low frequency earthquakes near parkfield, california: Implications for fault mechanics within the brittle-ductile transition, *Journal of Geophysical Research: Solid Earth*, *117*(B5).

Thomas, A., N. Beeler, Q. Bletery, R. Burgmann, and D. Shelly (2018), Using low-frequency earthquake families on the san andreas fault as deep creepmeters, *Journal of Geophysical Research: Solid Earth*, *123*(1), 457–475.

Thomas, A. M., G. C. Beroza, and D. R. Shelly (2016), Constraints on the source parameters of low-frequency earthquakes on the san andreas fault, *Geophysical Research Letters*, *43*(4), 1464–1471, doi:10.1002/2015GL067173.

Thompson, B. (2014), Okada wrapper, *Github Repository*.

Uchida, N., and R. Bürgmann (2019), Repeating earthquakes, *Annual Review of Earth and Planetary Sciences*, *47*, 305–332.

Wyatt, F., K. Beckstrom, and J. Berger (1982), The optical anchora geophysical strainmeter, *Bulletin of the Seismological Society of America*, *72*(5), 1707–1715.

Corresponding author: B. G. Delbridge, Department of Earth and Planetary Science, University of California Berkeley, 307 McCone Hall, Berkeley, CA 94703, USA. (delbridge@berkeley.edu)

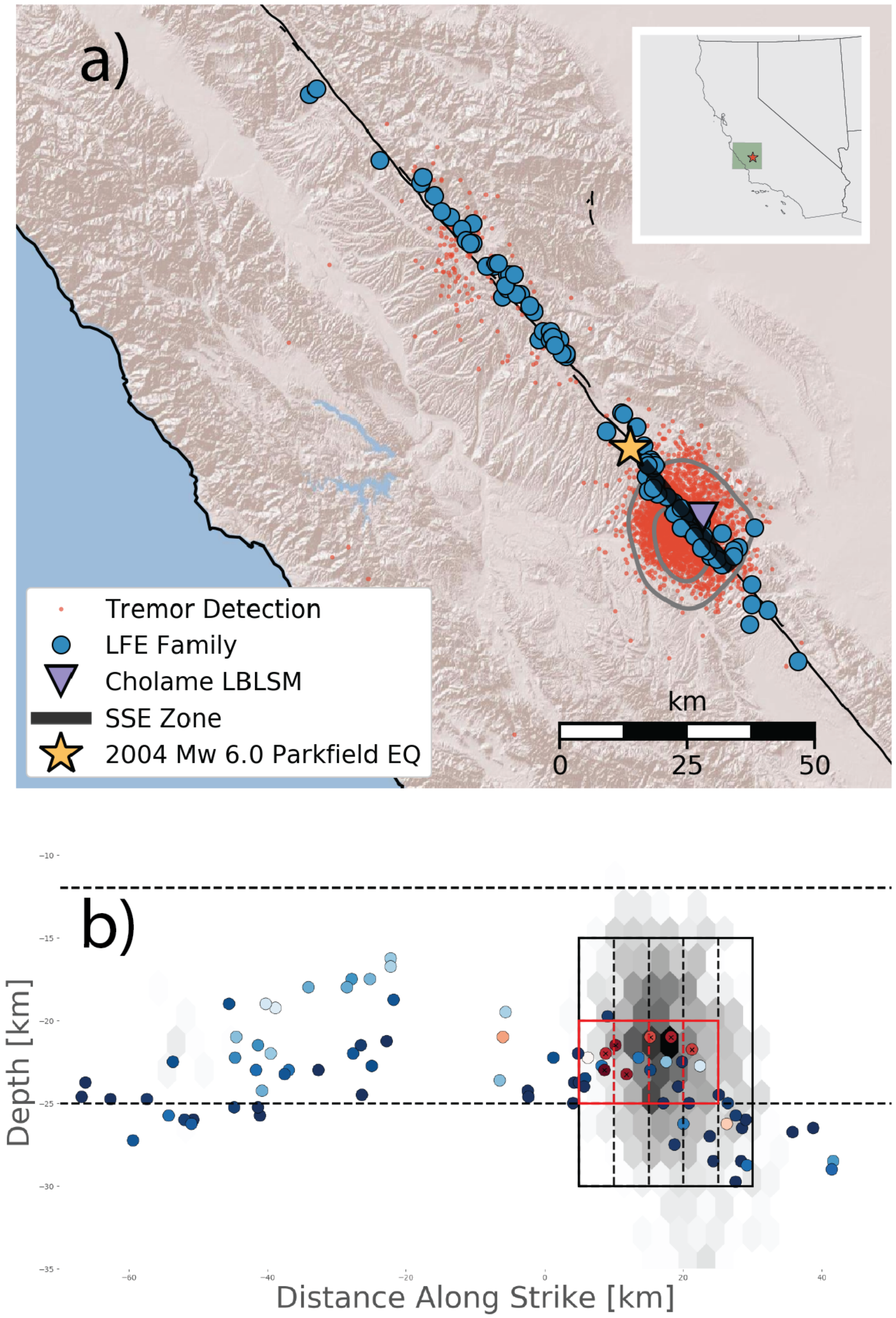
a)
Tremor Detection
LFE Family
Cholame LBLSM
SSE Zone
2004 Mw 6.0 Parkfield EQ
km
0
25
50
b)
Depth [km]
−10
−15
−20
−25
−30
−35
−60
−40
−20
0
20
40
Distance Along Strike [km]

Figure 1. Map and transect view of inferred Parkfield slow-slip region. a) The red circles denote tremor detections and blue circles denote the location of LFE Families identified by *Shelly* [2017]. The grey curves represent minimum contours which contain 95% and 50% of the Cholame tremors. The thick black line represents the surface trace of the inferred slow slip region (A) which shown in transect view in the panel below (Figure 1b). The gold star denotes the Mw 6.0 2004 Parkfield Earthquake epicenter. The triangle symbol denotes the location of the two long-baseline laser strainmeters CHL1 (oriented North-South) and CHL2 (oriented east-West). b) The x-axis denotes distance along strike, with the origin at the location of the 2004 Parkfield Earthquake, and the y-axis denotes depth. The black and red rectangles denote the slip areas (A) described in the main text as Model 1 and Model 2, respectively. The grey hexagons represent tremor density within 5 km of the fault with darker regions denoting higher tremor density. The circles represent the location of LFEs, with color denoting episodicity as measured by the minimum fraction of days which contain 75% of the tremor activity, warm colors (e.g. red) indicate highly episodic families, where as cooler colors (e.g. blue) denote more continuous behavior. The “highly-episodic” families are denoted by black x’s. The upper and lower dashed horizontal black lines denote the down-dip extent of the seismogenic zone and the Moho [*Ozacar and Zandt*, 2009], respectively.

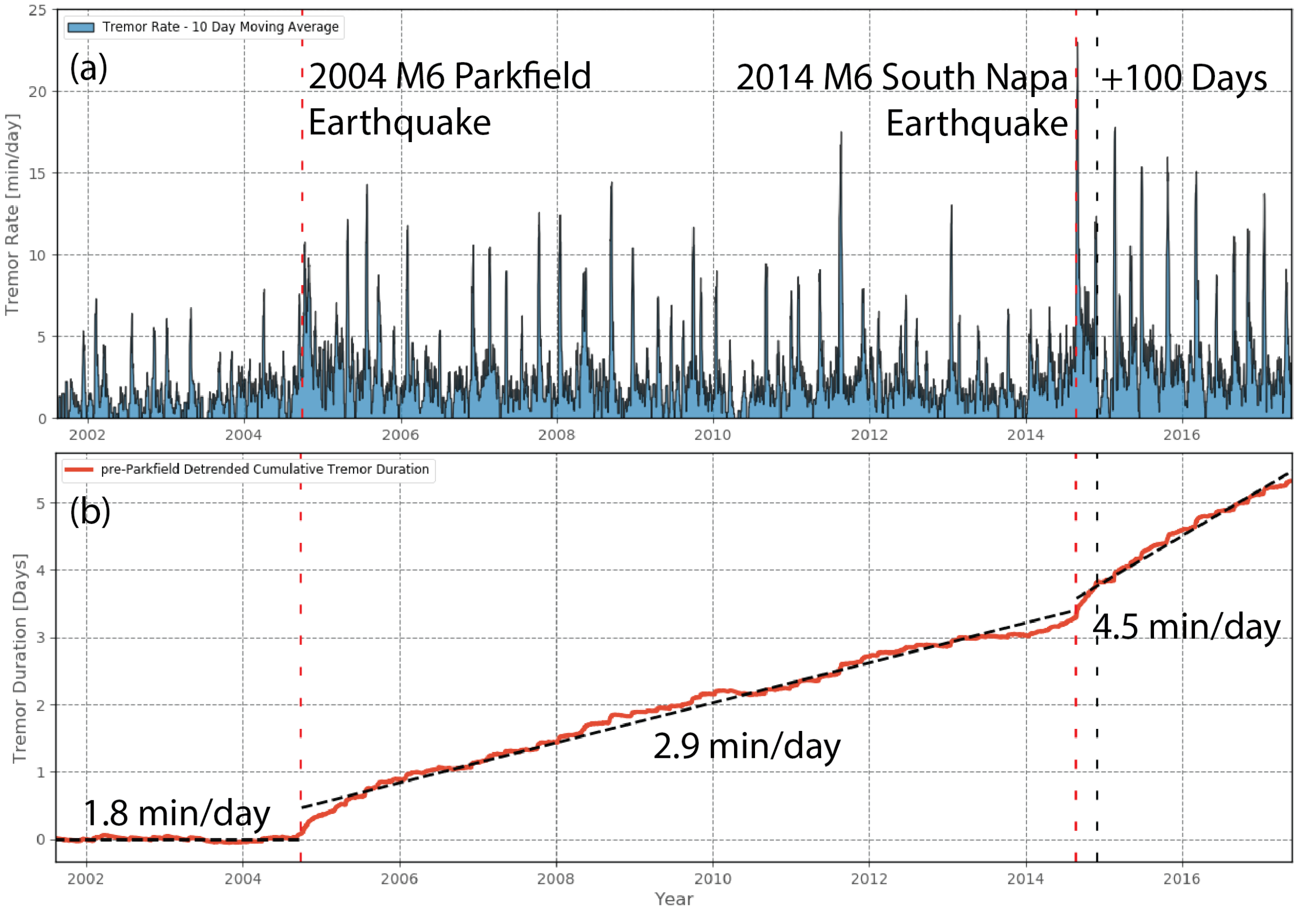

Figure 2. Tremor rate and cumulative tremor duration timeseries. The vertical dashed red bars denote the origin times of the 2004 M_w6.0 Parkfield Earthquake and 2014 M_w6.0 South Napa Earthquake. a) The blue curve represents a 10-day moving average of the tremor rate [min/day]. b) The red curve represents the cumulative tremor duration detrended by the pre-Parkfield Earthquake tremor-duration rate.

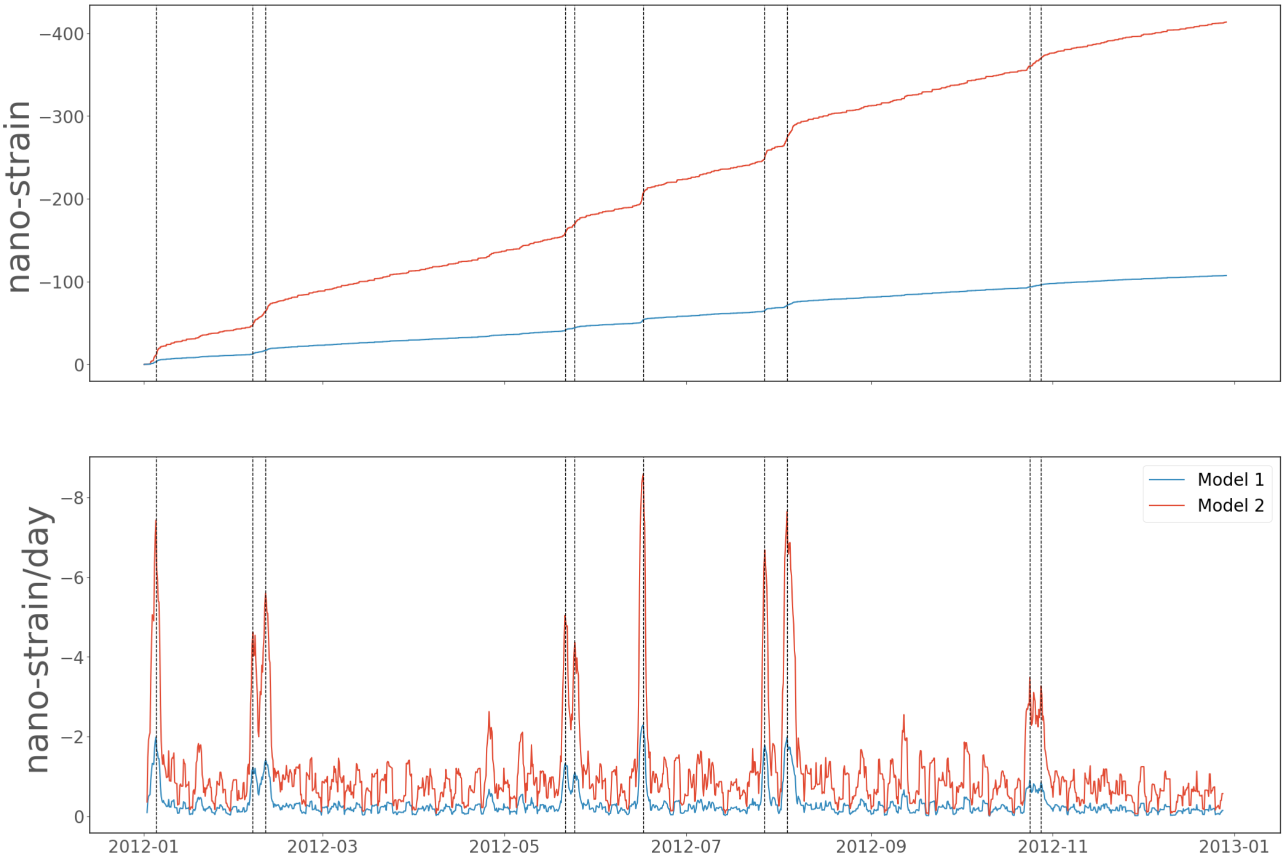

Figure 3. Modeled North-South surface strain at the long-baseline strainmeter calculated using five rectangular Okada dislocations with slip assigned to each LFE occurrence using equation 5. The blue and red curves represent the surface strain assuming the rupture areas in models 1 and 2 respectively (See Figure 1b). The top panel shows the raw strain time series, and the lower panel shows the strain-rate time series. The vertical black lines denote times of identified strain-rate peaks. Note that the results for the East-West strain are qualitatively the same, but with opposite sign.

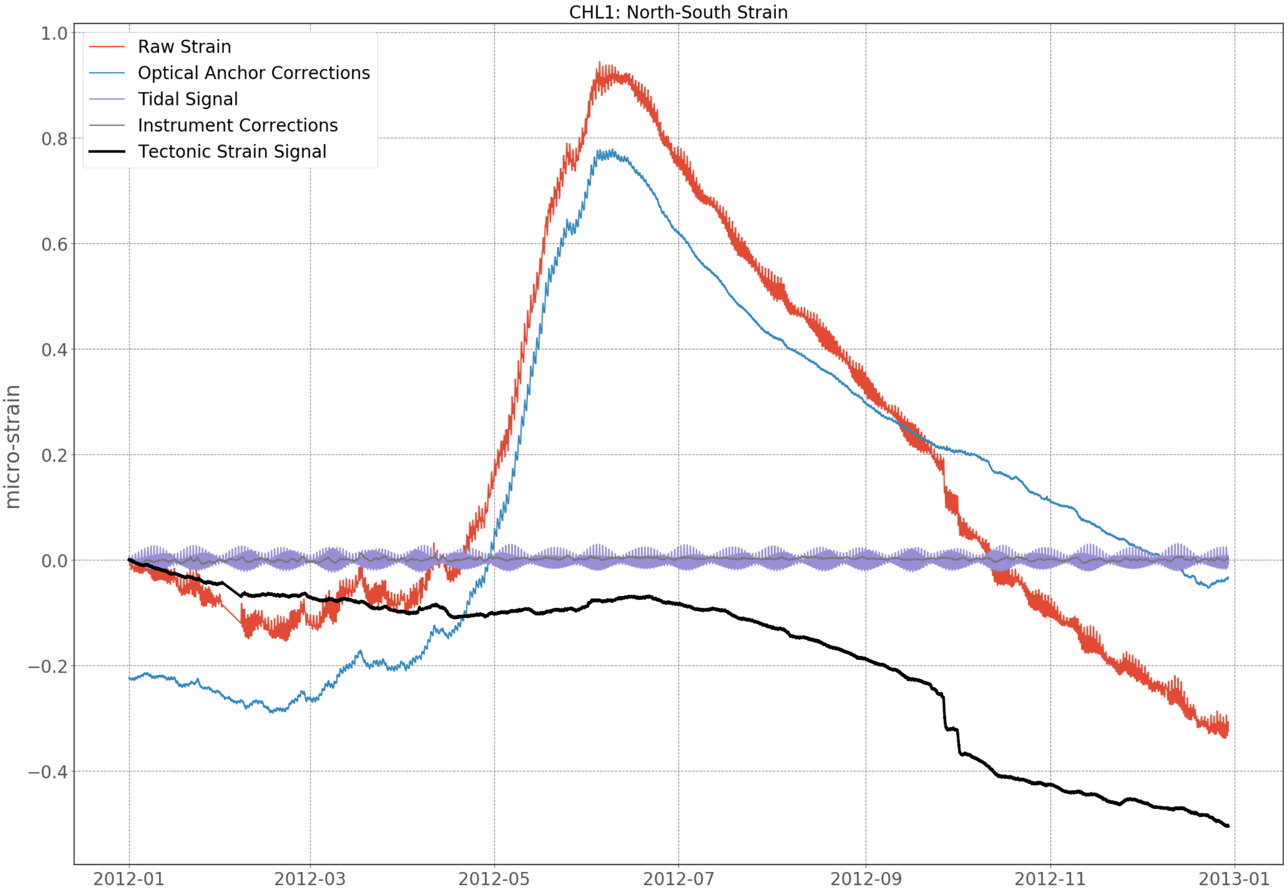

Figure 4. A yearlong North-South strain time-series measured at Station CHL1. The red curve shows the raw strain measured by the instrument. The blue curve shows the component of raw strain due to motion of the end point monuments. The grey curve corresponds to the component of raw strain attributable to instrument corrections. The purple curve shows the estimated tidal signal. The black curve shows the observed strain following corrections described in text.

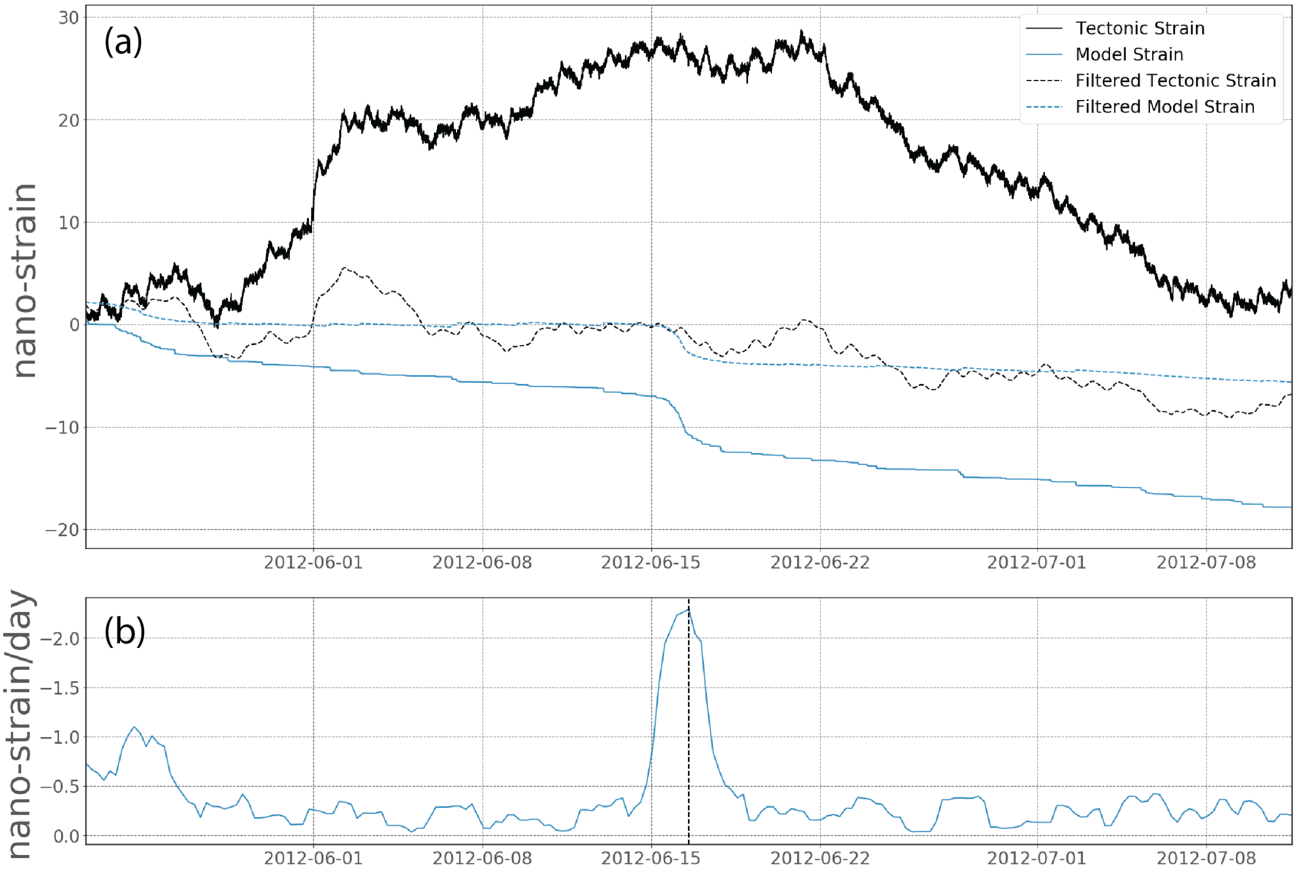

Figure 5. Comparison of the 50-day raw and processed LSM data with the raw and processed Model 1 derived synthetic strain centered about the time of the strain-rate peak identified on 2012-06-16 (The largest peak in Figure 3). The black and blue curves correspond to the LSM derived observed strain and the Model 1 synthetic strain respectively. The vertical dashed line denotes the time of the peak strain-rate. a) The solid and dashed lines represent the raw and filtered signals respectively. b) The strain-rate estimated from the Model 1 derived synthetic strain timeseries.

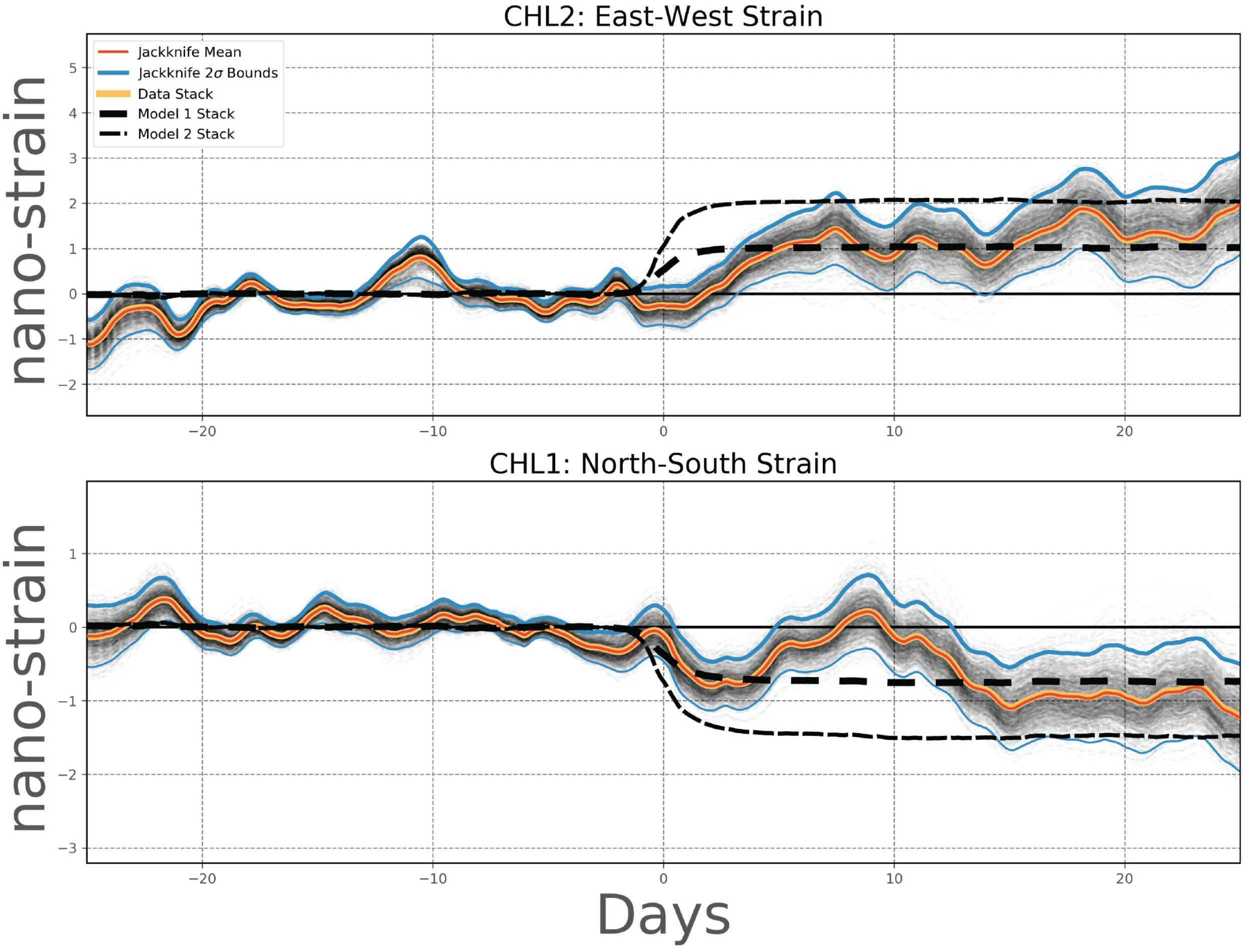

Figure 6. Stacked strain signals for all inferred slow-slip events observed at the two long-baseline laser strainmeters at Chalome, CA (Figure 1). The yellow curve represents the strain timeseries obtained from stacking the strain data associated with all the available strain peaks. The individual semi-transparent grey curves show the results of a bootstrapping analysis where 10% of the time periods are removed before constructing the stacks. The red line represents the mean of the bootstrapped results at each time period, and the blue lines represent 2σ bounds. The thick and thin dashed black lines represent the stacked modeled strain assuming the ruptures areas of Model 1 and Model 2 (denoted by the red and black rectangles in Figure 1b respectively.)

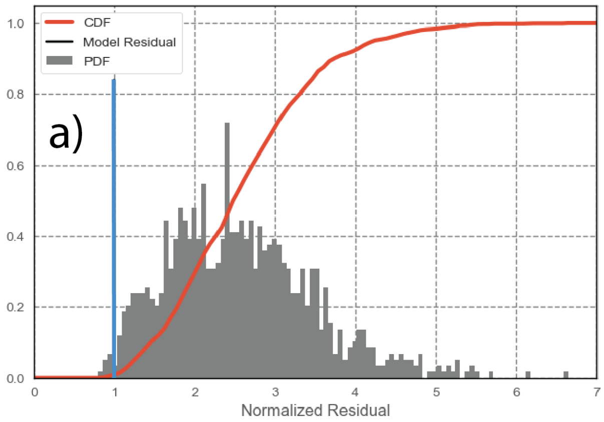

Figure 7. Distribution of random stack residuals. The grey bars denote the probability density and the red curve denotes the cumulative distribution. The vertical black bar denotes the values associated with the data stack and Model 1. a) Sum of the squared error of the random stacks from Model 1 normalized by the data stack's error. b) Simultaneous misfit of the means of the long term offsets from channels CHL1 and CHL2.

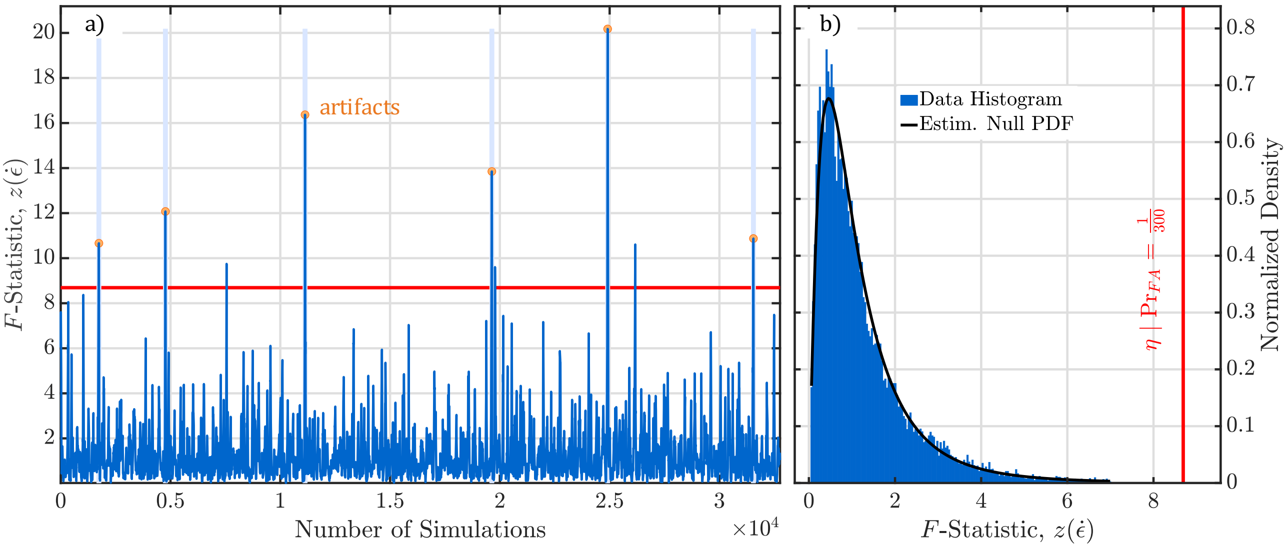

Figure A1. Test statistics from $\sim 3.3 \cdot 10^4$ randomized stacks of 44 CHL1 observed strain-rate data. **a**: A time series of $z(\dot{\epsilon})$ shows the ratio of two sample variance estimates of post-processed strain-rate $\dot{\epsilon}$ measurements collected from CHL1 (Equation A3). Samples of $z(\dot{\epsilon})$ that exceed the horizontal red line (η) mark where a test statistic has $< \frac{1}{300}$ chance of being observed in the typical background strain. **b**: A normalized histogram shows the empirical density function of $z(\dot{\epsilon})$ at left, overlain with its predicted central $\mathcal{F}$ PDF (black curve). The false detection constraint ($\Pr_{FA} = \frac{1}{300}$) determines the threshold η (red, vertical line). Orange circles mark peaks that exceed the threshold and indicate end of file artifacts that we reject as inconsistent with the assumptions of our hypothesis test. The few remaining detections are statistically expected from the false alarm rate.

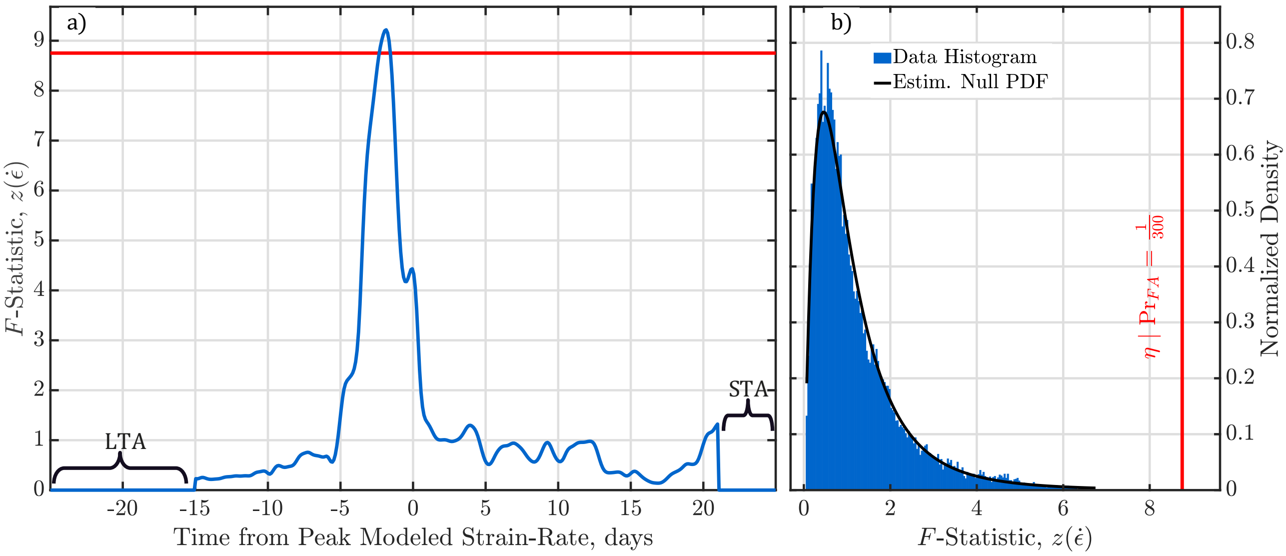

Figure A2. Test statistics for a stack of 44 CHL1 tectonic signals that we aligned to the peak modeled strain-rate that is predicted by Model 1 to follow slow slip events. **a**: The statistic $z(\dot{\epsilon})$ for a possible geodetic signal. The beginning and end of each time series show zero values where the long-term window (10 days) and short-term window (4 days) do not fully overlap the data. The horizontal line marks the threshold set by the same $\mathrm{Pr}_{FA} = \frac{1}{300}$ false alarm rate in Figure A1b. **b**: The histogram of the background observed strain rate and the predicted null PDF that predicts the threshold η, duplicated from Figure A1b.

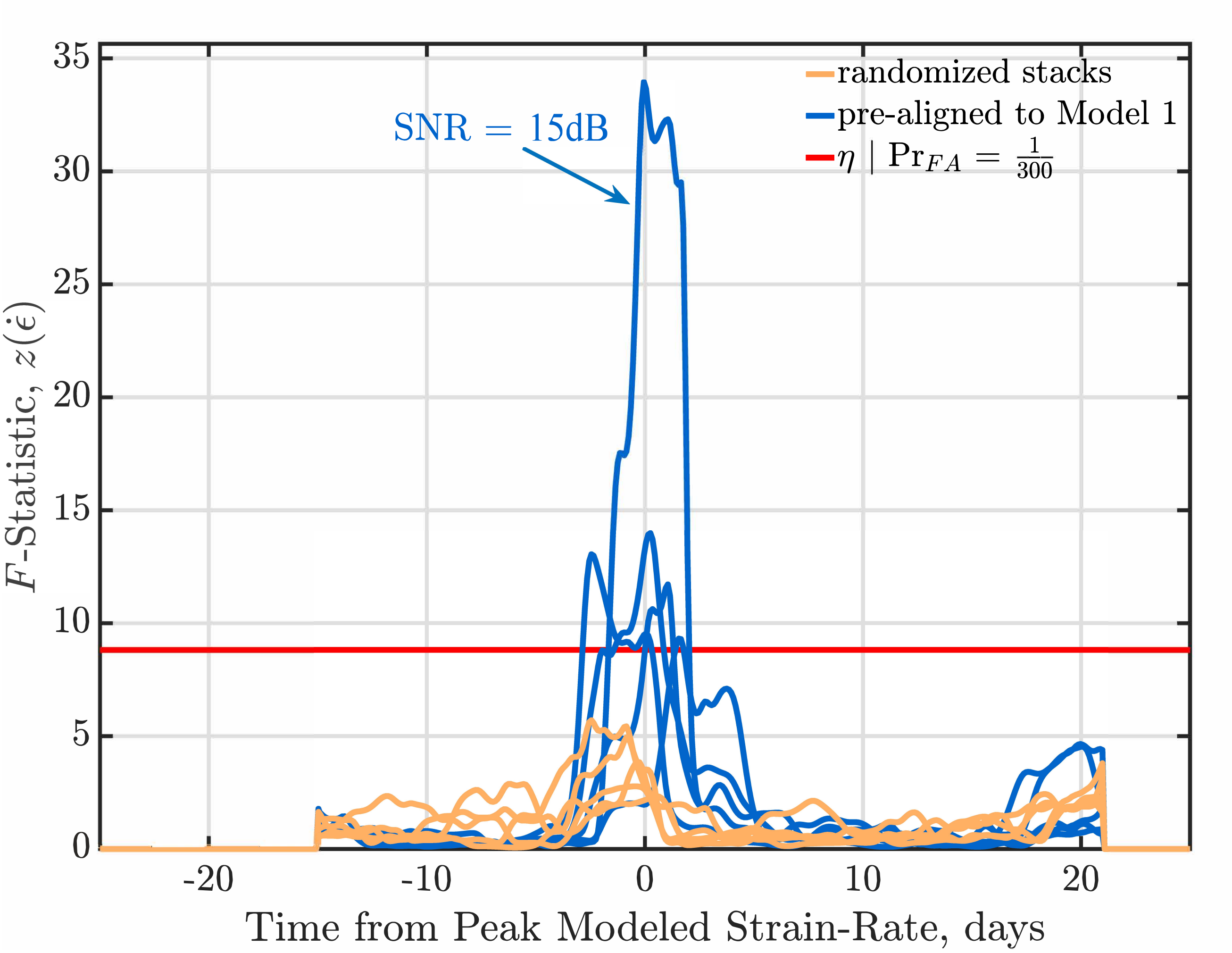

Figure A3. Test statistics for 44 CHL1 observed strain-rate signals that are phase shifted and then stacked. Phase shifts are randomly sampled from a uniform distribution of $\leq \pm 2$ days, 10^4 times. Blue curves show five of 10^4 realizations of the test statistic that processed strain-rate data for 44 observations that we pre-aligned to peak modeled strain-rate, then re-shifted and stacked. Orange curves show five of 10^4 realizations of the test statistic that processed 44 observations of random realizations of strain-rate data that we similarly shifted and stacked. The threshold η (red line) matches that in Figure A2 and Figure A1. Both cases (blue and orange) show the five largest values of $z\,(\dot{\epsilon})$ among the 10^4 realizations. Peaks that exceed the threshold are evidence that a geodetic signal is present in the stack of 44 records. Figure A2 describes the leading and ending zero data. The peak SNR $(\sum_t^S \dot{s}_t^2 \;/\; \sum_t^S n_t^2)$ has units of decibels $(10 \log_{10} (\mathrm{SNR}))$.